

Lawrence Berkeley National Laboratory

Lawrence Berkeley National Laboratory

Title

Stereo soft x-ray microscopy and elemental mapping of hematite and clay suspensions

Permalink

<https://escholarship.org/uc/item/1cs6w25h>

Author

Gleber, S.-C.

Publication Date

2008-11-25

Stereo soft x-ray microscopy and elemental mapping of hematite and clay suspensions

S.-C. Gleber¹, J. Thieme¹, W. Chao², P. Fischer²

¹Institute for X-ray Physics, Georg-August-University, Friedrich-Hund-Platz 1,
37077 Gottingen, Germany

²Lawrence Berkeley National Lab, Center for X-ray Optics, Berkeley, CA 94720
USA

This work was supported by the Director, Office of Science, Office of Basic Energy Sciences, of the U.S. Department of Energy under Contract No. DE-AC02-05CH11231.

Stereo soft X-ray microscopy and elemental mapping of hematite and clay suspensions

S.-C. GLEBER¹, J. THIEME¹, W. CHAO², P. FISCHER²

¹ *Institute for X-ray Physics, Georg-August-University, Friedrich-Hund-Platz 1, 37077 Göttingen, Germany*

² *Lawrence Berkeley National Lab, Center for X-ray Optics, 1 Cyclotron Road, Berkeley, CA 94720 U.S.A*

Summary

The spatial arrangements of hematite particles within aqueous soil and clay samples are investigated with soft X-ray microscopy, taking advantage of the elemental contrast at the Fe-L edge around E=707 eV. In combination with stereo microscopy, information about spatial arrangements are revealed and correlated to electrostatic interactions of the different mixtures. Manipulation of a sample mounted to the microscope is possible and particles added while imaging can be detected.

Introduction

Soft X-ray microscopy has become a mature analytical tool with various applications to nanoscale behavior in materials, environmental and biological sciences. A compendium of the achievements can be found e.g. in Susini *et al.* (2003) and Aoki *et al.* (2006). Recording

the X-ray images within the so-called water window, i.e. using photon energies between the K-absorption edge of oxygen ($E \approx 530$ eV or $\lambda = 2.34$ nm) and carbon ($E \approx 280$ eV or $\lambda = 4.43$ nm), are especially suitable for imaging samples in aqueous media (Wolter, 1952). The optimum optical thickness is determined by the $1/e$ ratio of the transmitted radiation, which in the water window extends up to $10\text{ }\mu\text{m}$ around the oxygen K-edge (Kirz *et al.*, 1995). Since spatial resolution scales with the wavelength, soft x-ray microscopy enables high resolution transmission images of much higher spatial resolution compared to optical microscopy. Currently the best spatial resolution in soft X-ray microscopy has been achieved down to 15 nm resolution (Chao *et al.*, 2005). This gives a unique way of studying biological or environmental samples in their natural aqueous state without staining or fixation. By changing the incident X-ray energy and taking one image above and one below an absorption edge, the distribution of the element corresponding to the absorption edge can be visualized. This can be done either by just comparing the images and identifying the stronger absorbing structures or by creating a map of the elemental distribution by dividing these two images.

Iron is an abundant cation in soils and groundwater aquifers. It can occur bivalent or trivalent, depending on the redox condition. Ferrous iron, Fe^{2+} , is abundant under anaerobic conditions but unstable in aerobic conditions. At the groundwater surface or by mixing of anaerobic bankfiltrate and aerobic water the groundwater may get in contact with oxygen. Iron will be oxidized to ferric iron, Fe^{3+} , a source for precipitation. It gives rise to the formation of new colloidal particles (Hofman *et al.*, 2003). An increasing formation of ferric hydrates causes turbidity in soil water and groundwater and is considered harmful. The use of water for engineering purposes containing too much iron may cause corrosion and the deposition of colloidal sized iron particles. The two most abundant colloidal iron oxides in soils are goethite, needle-like crystals, and hematite, hexagonal platelets, followed by the poorly crystallized hydrous ferrihydrite (Sparks, 1995). The colloid fraction in soils, mainly clays, oxides, and

organic substances, show significant effects on many soil chemical processes due to their high specific surface areas and especially in the micro pore system built with colloids. The surface of these colloids is charged, clays as well as humic substances show within a wide pH-range ($3 \leq \text{pH} \leq 8$) negative charges, whereas iron oxides are positively charged in the same range. Therefore, iron oxides are able to bind other soil particles forming a micro texture. Small iron oxide particles might penetrate the formerly loose colloidal matrix and solidify it due to electrostatic interaction. A change in the texture of the microstructure of soils, which means to change the morphology of associations of soil colloids, influences e.g. runoff and erosion losses within soils. The relationship between iron oxide and the stability of soil colloid associations is however still debated in soil science, e.g. by Duiker *et al.* (2003) or Rhoton *et al.* (2003).

Materials and methods

For the studies presented here, the high resolution full field soft X-ray transmission microscope of the Center for X-Ray Optics located at beamline 6.1.2 of the Advanced Light Source, Lawrence Berkeley Laboratory, Berkeley, has been used (Meyer-Ilse *et al.*, 2000; Fischer *et al.*, 2006; Thieme *et al.*, 2003). The X-ray optical set-up of this transmission X-ray microscope consists of Fresnel optics for both the condenser zone plate and the micro zone plate as shown in Fig. 1. The condenser zone plate collects the synchrotron radiation emitted from a bending magnet and focuses it onto the object. In addition, it works in combination with the pinhole in front of the object as a linear monochromator (Niemann *et al.*, 1974). It reduces the bandwidth of the radiation illuminating the object to about $E/\Delta E \approx 500$. A micro zone plate downstream the object acts as a high resolution X-ray objective and forms an enlarged image

of the object in the image plane. The image is recorded with a backside illuminated slow-scan CCD-camera. Exposure times are typically in the range of several seconds. For the experiments, a micro zone plate with an outermost zone width of $dr_n=25$ nm was used to take high resolution images around the Fe-L edge at approximately $E=707$ eV or $\lambda=1.75$ nm.

According to

$$\sigma = 1.22 \cdot dr_n$$

the lateral resolution is $\sigma \approx 30$ nm. With

$$\delta = 4 \frac{dr_n}{\lambda}$$

the depth of focus in the experiments has been $\delta \approx 1.43$ μm (Attwood, 1999). The magnification was about 2800. The CCD camera has been used either with 2048x2048 pixel or in a 1024x1024 binned mode, resulting in a pixel size of either 0.45 μm or 0.9 μm in the object plane. Thus, the images have been sufficiently oversampled in regard to the optical resolution.

Due to the high absorption in air of X-rays with such a low energy, the optical path has to be in vacuum. To allow for samples in aqueous media, the sample stage is therefore located in a small air gap between the vacuum chamber containing the condenser and the vacuum chamber holding micro zone plate and CCD camera. To optimize between X-ray transmission and sample handling, the gap is typically about 200 μm wide. Both chambers are sealed with Si_3N_4 windows typically 100 nm thick.

Of particular interest is to know the spatial arrangement within a sample environment just by distances or lengths. Tomography reveals the 3-dimensional structure and thus can be used to deliver such information. However, many pictures are needed and due to inevitable deterioration of the sample by radiation damage, cryo-fixation is mandatory. Instead, stereo imaging needs only two images to reveal distances between particles or lengths within a

sample. For this, the aqueous environment can be sustained under ambient temperatures. Especially for the investigation of the dynamics of colloidal structures it is necessary to keep the system aqueous. To reveal structural changes within a colloidal suspension as a function of time and / or a function of changing chemical conditions, this combination of ambient sample conditions and stereo imaging is very well suited.

The theory behind stereo calculations consists of the parallax equation. In two dimensions, when tilting an L-like structure around the z-axis vertical to the object plane as can be seen in Fig. 2, the coordinates of three points a,b,c are related as follows, where index 1 gives the coordinates of the projection of the counterclockwise tilted object, and index 2 of the clockwise tilted object with Θ as tilting angle. The line with the length s between a and b is parallel to the x-axis, the line with the length h between b and c is vertical to the x-axis.

$$\overline{a_1c_1} = \overline{a_2c_2} = s \cdot \sin \theta \quad \text{and} \quad \overline{b_1c_1} = \overline{b_2c_2} = h \cdot \sin \theta$$

$$s_1 = \overline{a_1c_1} = s \cdot \cos \theta - h \cdot \sin \theta \quad \text{and} \quad s_2 = \overline{a_2c_2} = s \cdot \cos \theta + h \cdot \sin \theta$$

$$\Rightarrow h = \frac{s_2 - s_1}{2 \sin \theta} = \frac{\Delta Y}{2 \sin \theta}$$

Thus, the parallax equation relates the parallax ΔY to the vertical distance h and the tilting angle 2θ (θ is the stereo angle).

More general and for a 3 dimensional object, the coordinates (X, Y, Z) of one point are related as follows to the projection coordinates of that point in two images, (x_1, y_1) and (x_2, y_2) , in which the object is projected onto the x-y-plane and tilted by $\Theta_2 - \Theta_1 = \Theta$ around a tilting axis parallel to the x-axis (Fig. 3).

$$\begin{bmatrix} x_1 \\ y_1 \end{bmatrix} = \begin{bmatrix} X \\ Y \cos \theta_1 + Z \sin \theta_1 \end{bmatrix} \quad \text{and} \quad \begin{bmatrix} x_2 \\ y_2 \end{bmatrix} = \begin{bmatrix} X \\ Y \cos \theta_2 + Z \sin \theta_2 \end{bmatrix}$$

Setting the relation of the depth h from the 2-dimensional description as Z for the 3-dimensional object, the spatial coordinates of the point are determined as

$$X = x_1 = x_2, \quad Y = \frac{y_1 + y_2}{2 \cos \theta}, \quad Z = \frac{y_1 - y_2}{2 \sin \theta}$$

X-ray images can be assumed as parallel projections as long as the longitudinal extension of an object is smaller than the depth of focus of the used micro zone plate (Weiβ *et al.*, 2000).

Based on this assumption and on the parallax equation, the program XSTEREO has been written in IDL to mark or select prominent structures in a set of tilted X-ray images and to get information about the 3-dimensional configuration, distances and lengths (Gleber *et al.*, 2003).

Matching points recognizable in both projections are marked manually. An additional feature of the program allows for connecting these points with lines. The spatial coordinates of each pair of matching points are calculated and the points or lines are presented in a 3-dimensional plot. By free hand drawing, structures like edges can also be marked in both images and are then reconstructed point by point. In the 3-dimensional plot, features like curvatures are displayed. The distances of all chosen structures are given in user-defined units.

As tiltable holders for experiments with aqueous samples thin-pulled glass capillaries can be used, which are already common for tomography (Lehr, 1997; Schneider *et al.*, 2002; Larabell *et al.*, 2004). For these studies, borosilicate glass capillaries (*Hilgenberg*) of 1 mm outer diameter and 0.1 mm wall thickness were used. For easier filling, the capillaries have a 0.1 mm thick glass filament attached to the inner wall, improving the capillary forces when filled with a liquid. Capillary tips down to diameters of 1 μm and lengths short enough to stay stable without movements in the microscope have been produced with a pipette puller (*H. Saur*).

The thick base of the capillary is mounted into a steel tube which is fixed to the actual object

holder of the X-ray microscope (Fig. 4a). A cock wheel attached to the end of the steel tube allows for rotation of the capillary along an axis perpendicular to the optical axis either manually or using a motor. The air gap is about 200 μm wide, ensuring the tilt of the capillary over the whole range of 180 degrees without hitting a vacuum window even when the rotation axis is slightly mismatched. The X-ray transmission of a capillary with a diameter of 2 μm , which has subsequently a wall thickness of 0.2 μm , filled with water, can be calculated to 2.5 % at E=700 eV.

The full tilt range cannot be covered with an extended sample holder, which is however advantageous for studying extended objects. Small tilting angles are sufficient for stereo imaging, so it is possible to place an aqueous sample into the X-ray microscope in a tiltable flat holder. Herefore, two Si_3N_4 membranes (*Silson Ltd UK*) of 100 nm thickness each, have been used. The dimensions of the Si_3N_4 foils are comparable to these of the Si_3N_4 foils acting as vacuum windows, thus limiting the usable tilt range. With the sample in between, a pair of foils is glued across a 1 mm hole onto a 100 μm thin aluminum foil, which is mounted to the microscope in a way similar to the capillary mounting (Fig. 4b). The maximum tilt range between the two vacuum windows of the microscope is approximately 14 degrees. This is sufficient to obtain images for stereo analysis.

To avoid drying of the samples during the experiments, holders of both types have to be sealed. The tips of the capillaries were carefully dipped into a drop of silicon glue after filling. For the studies of extended objects, a drop of the aqueous sample was placed onto one of the Si_3N_4 foils and than covered with the other one. Due to capillary forces, the water layer between the two foils adjusts to the micrometer range. Using a pair of Si_3N_4 foils enclosing a water layer of 2 μm thickness yields a calculated X-ray transmission at E=700 eV of 8.5 %. The pair of foils has been sealed with glue around the edge of the wafers and subsequently fixed onto the aluminum foil.

The samples for these experiments have been limited to two iron oxides and two clay minerals, all very abundant in the environment, and a well characterized soil. The iron oxides were hematite and goethite (*Sigma Aldrich*, CAS number 20344-49-4), montmorillonite and caolinite were chosen as clay samples, and chernozem as a soil (Ahl *et al.*, 1985). All samples have been used as 1% (w-w) dispersion in deionized water. Thus, large clusters of colloids disaggregate to small clusters with an intact nano- and microstructure which can be imaged very well in an X-ray microscope. Hematite particles with approximately 150 nm diameter have been made according to Schwertmann and Cornell (2000) and supplied as well as montmorillonite and caolinite by J. Niemeyer, Institute for Soil Science, University of Göttingen.

Results

Fig. 5 shows a X-ray micrograph of an aqueous chernozem sample where hematite has been added. As extended clusters of soil colloids were expected, the flat holder has been used for this experiment. The left image was taken at $E= 704$ eV below the iron K-absorption edge, the right one shows the same region but taken at the absorption maximum at 710 eV. Exposure times for both images were 7.2 seconds with 2048x2048 pixels. The energies have been chosen according to peak position of L-3 edge of hematite (Garvie & Buseck, 1998). The pair of images shows a part of a cluster with a large particle in the image center, probably a clay particle. When comparing both images, the ferruginous hematite particles can be identified clearly in the right image, so it is not necessary to create elemental distribution maps dividing the images. It is noticeable that the hematite is located just at the edge of the large clay particle. This is an indication for an electrostatic interaction of the positively charged hematite

particles with the negatively charged edges of the clay platelets.

Fig. 6 shows clusters of caolinite platelets within one sample mixed with hematite also between two Si_3N_4 foils. The images on the left side were again taken at 704 eV and the ones on the right side at 710 eV, exposure times were 9.5 seconds with 2048x2048 pixels. Again, the hematite particles are located at the edges of the negatively charged clay platelets, indicating electrostatic interaction.

In Fig. 7, a montmorillonite sample mixed with hematite between two Si_3N_4 foils and imaged at 700 and 707 eV can be seen. Exposure times were 0.45 seconds with 1024x1024 pixels. Although due to a slight mismatch in energy the contrast is not optimum, the hematite particles can be seen still in the right image when comparing it with the left image. This sample was then tilted 14 degrees around a horizontal axis and imaged again at the two energies. Fig. 8 shows cut-offs of the sample shown in Fig. 7, one selected from the right image of Fig. 7, the other one selected from an image of the same region taken at E=707 eV after tilting the sample. The discrimination between soil and hematite particles again was obvious. Hematite particles were identified and marked as dots, whereas nearby edges of clay platelets were marked as lines, and then processed with XSTEREO. The created plot of the three-dimensional arrangements of the marked structures is presented in three different viewing angles in Fig. 9. Note, that the units of this plot are pixels, with one pixel corresponding to 9 nm. Distances between the structures were determined. So, it became clear that the hematite particles, whose centers are marked as structures no. 2 (dark green) and 3 (blue), are attached to the edges of clay platelets, marked partially as no. 8 (dark magenta) and 9 (light magenta), respectively. The distances have been determined to 60 nm and 80 nm. Taking the radii of the hematite particles into account, this corresponds to a direct attachment. Hematite particle no. 1 (red) is not as close to the clay edge no. 7 (light magenta) as it seems in the left image of Fig. 8, but has a distance of 180 nm. The minimum distance

between the center of the hematite particle no. 4 (orange) and the platelet edge no. 11 (dark magenta) is 630 nm. This cannot be seen by simply looking at one transmission image, rather, these structures seem to be attached to each other. This holds true also for particle no. 6 (light green) and edge no. 10 (light magenta), where the real distance is 600 nm. This spatial arrangement is visualized in Fig. 9, where particles and edges are plotted in a 3-dimensional coordinate system. Here, the hematite particles no. 4, 5, and 6 seem to be in one plane, possibly attached to one of the support foils.

Also capillaries were filled and mounted to the X-ray microscope. Fig. 10 shows two images of a capillary tip filled with caolinite taken at E=707 eV with a 14 degree tilt angle between them. Exposure times were 0.32 seconds with 1024x1024 pixels. The tip was sealed by dipping it into a drop of silicon glue to prevent drying. Unlike Fig. 6 where bigger caolinite platelets lay parallel to the Si_3N_4 foils, the structures inside the capillary seem to be more needle-like because only smaller platelets could reach the tip of 1.5 μm diameter. These small platelets show a good absorption contrast only when oriented parallel to the x-ray beam. The platelets oriented perpendicular to the light absorb the x-radiation so weakly that they are not visible. So, it became impossible in this case to identify the same edges in both images of the tilted pair.

The upper image of Fig. 11 shows a cluster of particles of a goethite dispersion in a capillary of approximately 2.5 μm diameter taken at 710 eV with an exposure time of 0.85 seconds with 1024x1024 pixels. In the images below, micrographs are shown taken of the same region as above, but after hematite particles had been added to the capillary. The tilt angle between these two images is 44 degrees. When comparing the top image and the bottom image on the left side of Fig. 11, the higher density of the cluster after the addition of hematite is clearly visible, and hematite particles, which are of different shape and smaller than goethite particles, can be identified. The morphological changes of the shape of the particle clusters

are due to dynamics within the dispersion. The two images below were taken one hour after the addition of hematite.

In Fig. 12, details from the micrographs shown in Fig. 11 below are presented, where some edges and centers of the goethite and hematite particles have been marked. The right image is taken from a 3-dimensional plot of the marked structures, visualizing the distances between the clusters and the particles. The points no. 1 (red) and no. 2 (red) represent two corners of a goethite particle, so the connection (red line) between both points marks the edge. When comparing these images with the top image in Fig. 11, taken before the addition of hematite, it becomes clear that only the particles marked as no. 7 and no. 8 are hematite particles. Again, distances have been determined, e.g. the distance between the hematite particles no. 8 and the edge of the goethite particle mentioned above is approximately 250 nm.

Three systems have been studied, caolinite, montmorillonite, and the soil chernozem. It is known, that clay minerals show a negative surface charge in combination with positively charged edges at low pH values. When increasing this value, the edge charges change to negative as well. For caolinite, the point of zero charge, i.e. the transition from positive to negative, lies around $\text{pH} \approx 2.7\text{-}3.2$ (Appel *et al.*, 2003). The hematite dispersion used here was measured to $\text{pH} \approx 3\text{-}4$. The point of zero charge for hematite is around $\text{pH} \approx 8$, resulting in positively charged particles added to the caolinite dispersion. As the caolinite has been dispersed with deionized water at neutral pH, and only little quantities of hematite have been added, the pH of the mixture is approximately $\text{pH} \approx 5$. Thus, the edge charge of the caolinite is negative, resulting in an electrostatic attraction of the hematite particles to these edges. This can be seen in Fig. 6.

The chernozem soil has a measured pH of $\text{pH}=8.4$. Here, the edge charge of the clay platelets can be assumed to be negative. Again, an electrostatic attraction of these edges towards the hematite particles can be expected. The spatial arrangement of hematite particles

around the edges of the soil particles visible in Fig. 5 supports this expectation.

The montmorillonite dispersion has a pH of $\text{pH} \approx 5\text{-}6$, resulting in a pH of the mixture measured to $\text{pH} \approx 4$. So, the edges of the clay platelets and the hematite particles are charged equally.

The measured distances derived from Fig. 8 show a more complex situation. Apart from the three hematite particles apparently attached to one of the support foils, two particles are very close to the clay platelets. However, the montmorillonite consists in general of very small sized platelets. Thus, it is difficult to differentiate between clay platelet vertically oriented to the optical axis and a stack of small platelets of the same extension, but with an orientation of the single platelets parallel to the X-ray beam. Taking this into account, it is very likely that these two hematite particles are attached to the plane of the clay platelets.

Conclusion

The presented results show the potential of the X-ray microscope XM-1 for spectromicroscopy experiments of aqueous soil samples at the Fe-L edge around 707 eV.

The mechanical precision of this instrument is well matched to the demands of stereo microscopy. The insertion and the use of capillaries or tiltable flat holders was uncomplicated, both could be quickly accessed and tilted due to the air gap.

The usage of Si_3N_4 foils and capillaries as holders for aqueous soil samples to be transmitted with x-rays around the iron L-edge could be compared. Generally, for stereo images both, foils and capillaries, were suitable as holders for aqueous samples and stayed stable over several hours. Between two Si_3N_4 foils, large soil particles could be imaged. The extension of the soil particles along the optical axis made sure that the foils could not collapse, so there was throughout the experiment a water layer of several micrometer thickness, and the

arrangement of the smaller structures like the hematite particles was still undisturbed. However, large particles were aligned with the foils. This was not the case in the capillaries which do not force the sample particles at all. A fundamental drawback is however that capillaries are not accessible for large particles.

With these features, it was possible to take stereo images of a selected sample region at different energies, so that elemental and spatial information could be combined. Iron containing particles could be identified non-ambiguously, e.g. hematite particles within aqueous colloidal soil samples. Distances between single particles or platelets within the three-dimensional sample association could be determined using XSTEREO. Positions and structures of points and platelet edges could be calculated and visualized in an three-dimensional plot. The diffusion of hematite particles into an already existing cluster of goethite particles is an example for the ability of X-ray microscopy to study the dynamics within an aqueous colloidal system. When the morphology of the particles differs, the dynamics can be followed even without elemental contrast.

The electrostatic interaction of colloidal soil particles with either opposite or equal charges could be investigated directly in aqueous media. The surface charge of soil particles changes with the pH of the dispersion. When oppositely charged, it causes electrostatic attraction, e.g. between clay particles and iron containing particles. These electrostatic forces are weak, therefore particles have to be in close vicinity to each other to sense the electric field. The result of the electrostatic attraction was detected by identifying hematite particles close to edges of clay platelets. Thus, the consequences of different edge charges at certain pH values could be confirmed experimentally by direct imaging.

Acknowledgements

This work has been supported by the DFG under contract numbers Th445/8-1 and Th445/8-2. Operation of the soft X-ray microscope is supported by the Director, Office of Science, Office of Basic Energy Sciences, Materials Sciences and Engineering Division, of the U.S. Department of Energy. Thanks to J. Niemeyer, University of Göttingen, who prepared the hematite suspension. We would like to thank the staff of ALS and CXRO for providing excellent working conditions.

Figures

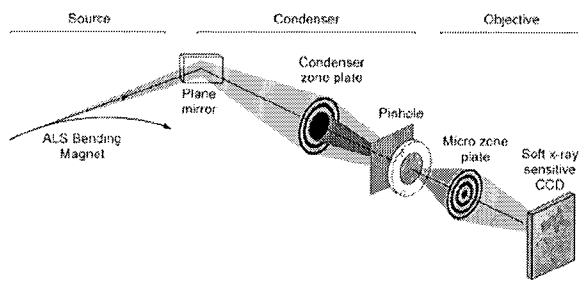


Fig. 1. Scheme of the X-ray microscope XM-1 at the Advanced Light Source, Berkeley, USA.
[Attwood (1999)].

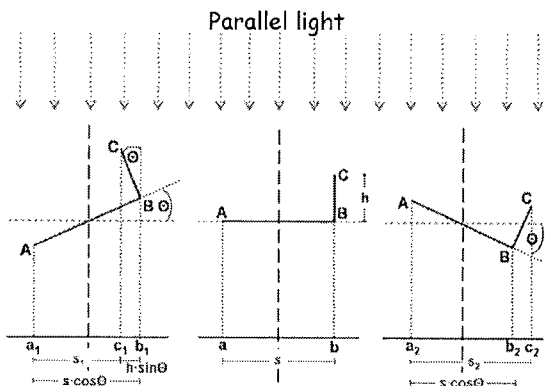


Fig. 2. Projection of a 2-dimensional object illuminated by parallel light

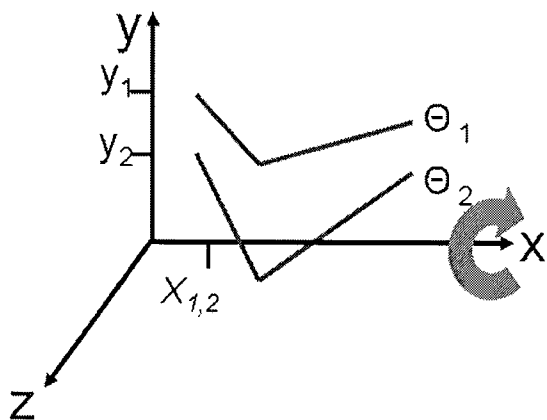


Fig. 3. Tilt of an object in three dimensions with the x-axis as rotational axis.

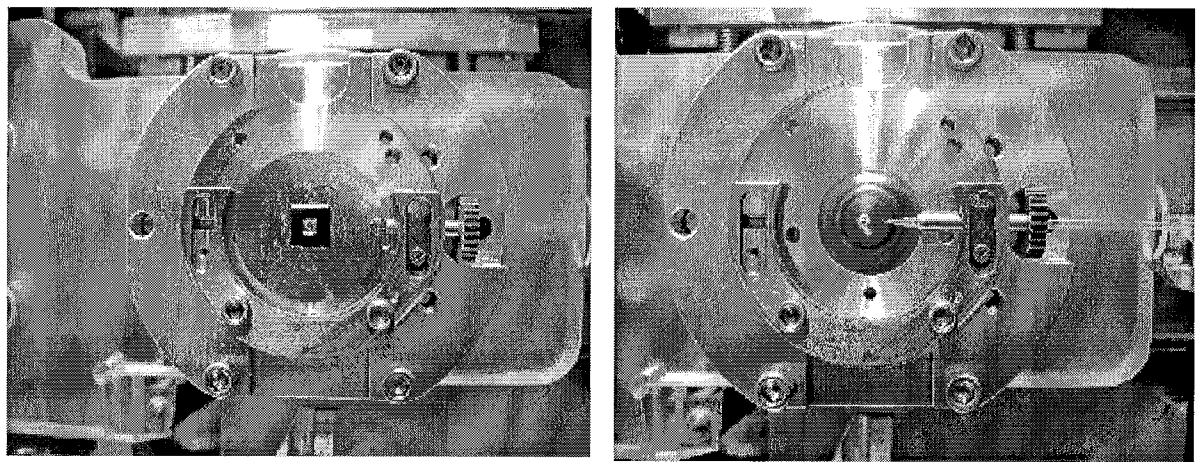


Fig. 4. Tiltable object holder mounted to the XM-1 object stage in front of the pinhole. *Left:* Thin- pulled glass capillary filled with a hematite suspension; *Right:* flat object holder consisting of a pair of Si_3N_4 foils.

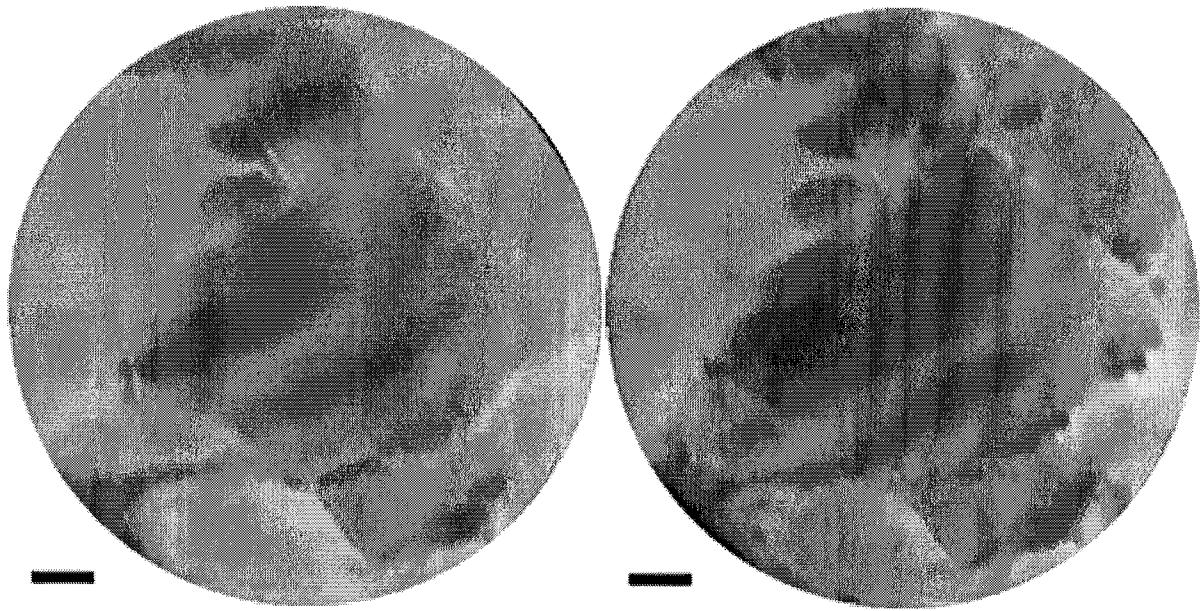


Fig. 5. Aqueous chernozem sample with hematite colloids between two Si_3N_4 foils; X-ray micrographs taken at $E = 704$ eV (*left*) and $E = 710$ eV (*right*). The scale bar in the left corner at the bottom indicates 500 nm.

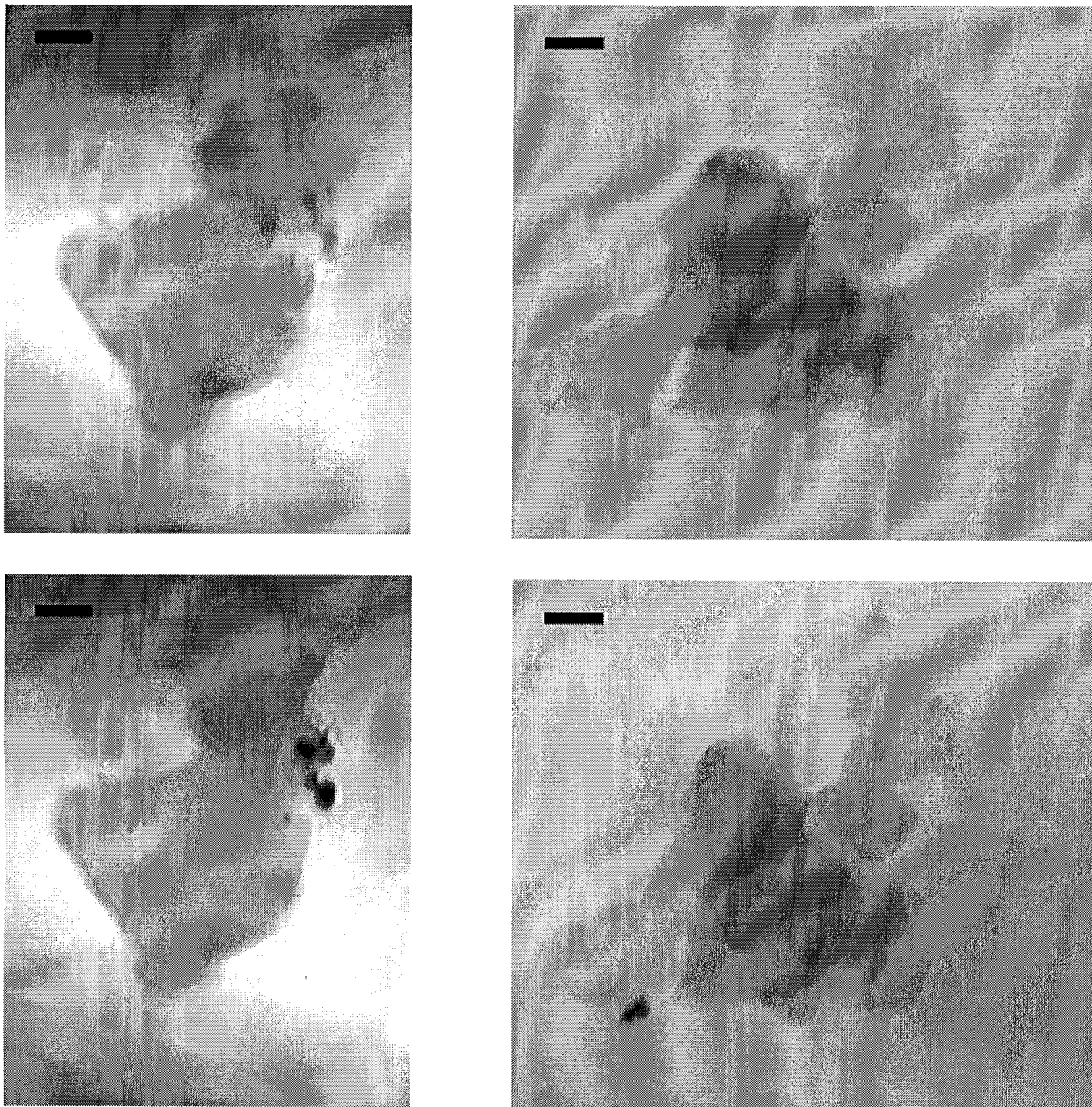


Fig. 6. Aqueous sample caolonite platelets with hematite colloids between two Si_3N_4 foils; images taken at $E = 704 \text{ eV}$ (*upper and lower left*) and $E = 710 \text{ eV}$ (*upper and lower right*). The scale bar in the top left corner indicates 500 nm.

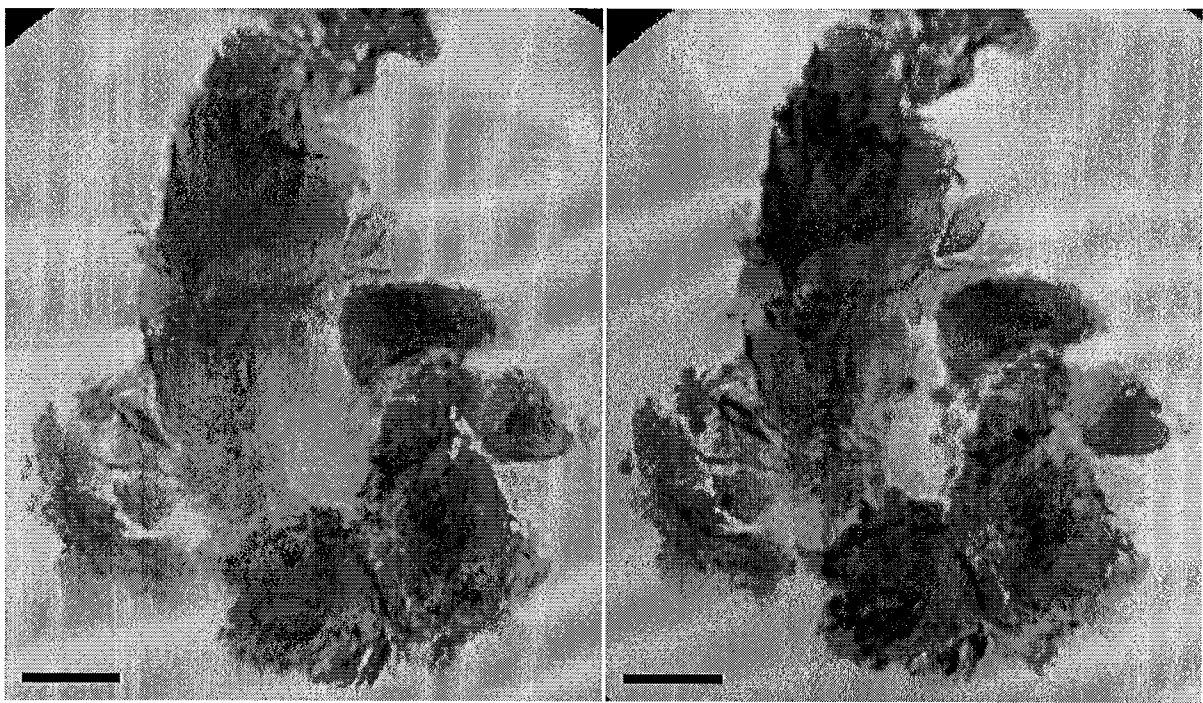


Fig. 7. Aqueous sample of montmorillonite particles with hematite colloids between two Si_3N_4 foils; images taken at $E = 700 \text{ eV}$ (*left*) and $E = 707 \text{ eV}$ (*right*). The scale bar indicates $1 \mu\text{m}$.

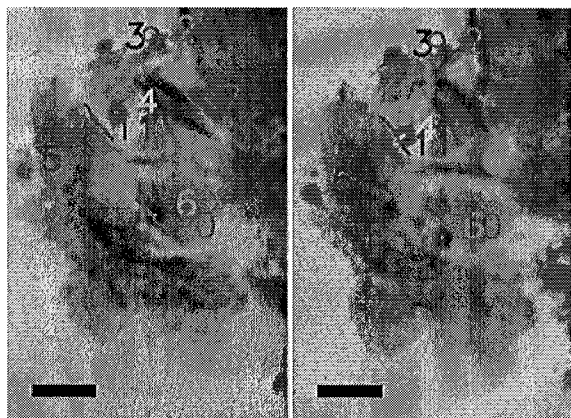


Fig. 8. Detail of the montmorillonite sample shown in Fig. 7 viewed with an angular difference between the images of 14 degrees around a horizontal tilt axis, taken at $E = 707 \text{ eV}$. Lines, points, and edges are marked for analysis. The scale bar indicates 500 nm .

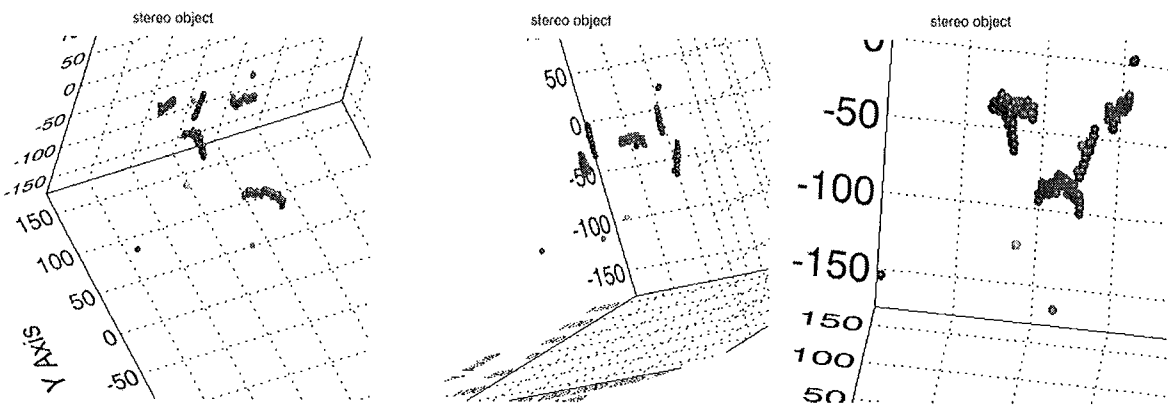


Fig. 9. Plot showing the points and edges marked in Fig. 8 under two different viewing angles.

The unit of the axis is pixels. In the used images, 10 pixels relate to 90 nm.

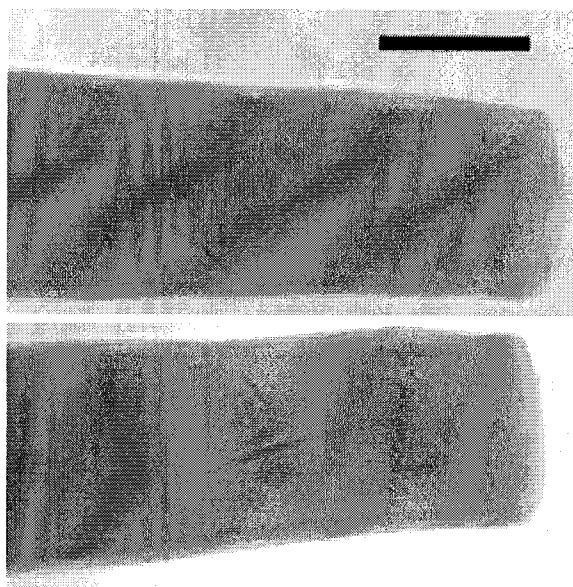


Fig. 10. Small particles of a caolinite dispersion in a capillary tip with approximately $1.5 \mu\text{m}$ diameter, taken at $E=707 \text{ eV}$. The tilt angle between the two images is 14 degrees, the scale bar is $1 \mu\text{m}$.

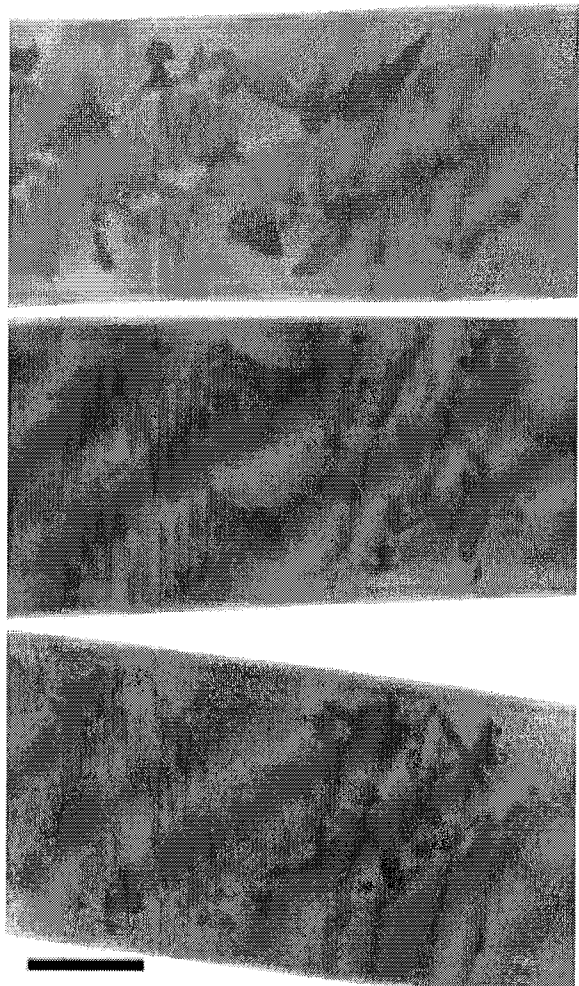


Fig. 11. *Top:* Cluster of particles of a goethite dispersion in a capillary of approximately 2.5 μm diameter taken at 710 eV. *Middle and bottom:* Same region as in the upper image after adding hematite particles to the capillary. The tilt angle between the middle and the bottom image is 44 degrees. The scale bar indicates 1 μm .

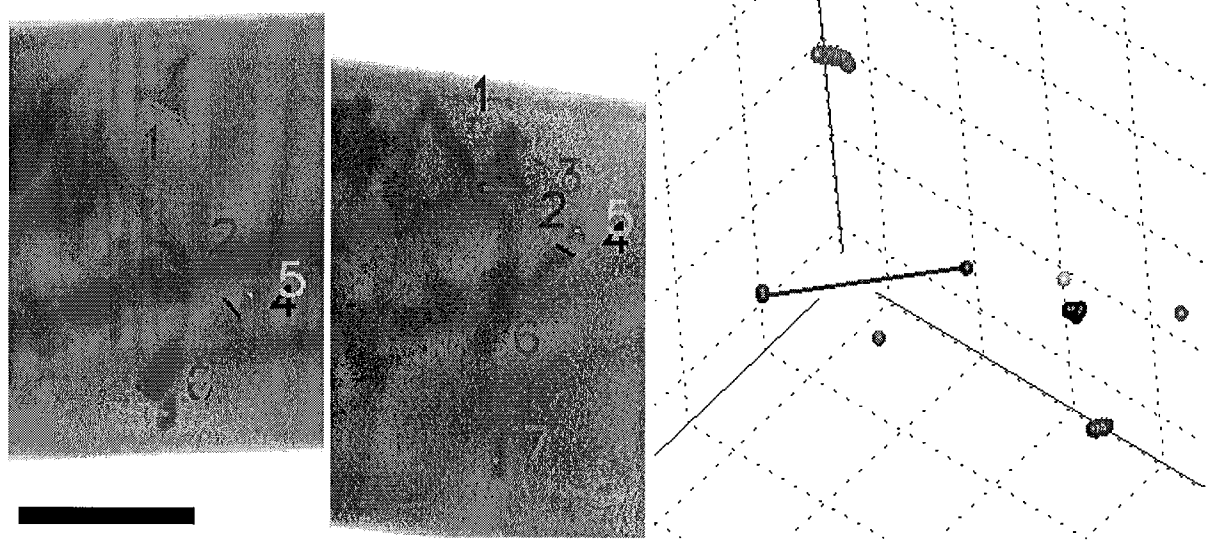


Fig. 12. *Left and center:* Details from the images shown in Fig. 11 bottom. Some edges and centers of the goethite and hematite particles have been marked. *Right:* Image of 3-dimensional plot of the marked structures.

References

- Ahl, C., Frede, H.-G., Gäth, S. & Meyer, B. (1985) Böden aus Löß des Leinetalgrabens und seiner Hochflächen-Umrandung. *Mitt. Dt. Bodenk. Gesellsch.*, **42**, 359-434.
- Aoki, S., Kagoshima, Y. & Suzuki, Y. (Eds.) (2006) Proceedings of the 8th international conference on X-ray microscopy. *IPAP Conference Series 7*, IPAP, Tokyo, Japan.
- Appel, C., Ma, L.Q., Rhue, R.D. & Kennelley, E. (2003) Point of zero charge determination in soils and minerals via traditional methods and detection of electroacoustic mobility. *Geoderma*, **113**, 77-93.
- Attwood, D.T. (1999) *Soft X-rays and extreme ultraviolet radiation*. Cambridge University Press, Cambridge.
- Chao, W., Harteneck, B.D., Liddle, J.A., Anderson, E.H. & Attwood, D.T. (2005) Soft X-ray microscopy at a spatial resolution better than 15 nm. *Nature*, **435**, 1210-1213.
- Duiker, S.W., Rhoton, F.E., Torrent, J., Smeck, N.E. & Lal, R. (2003) Iron (hydr)oxide crystallinity effects on soil aggregation. *Soil Sci. Soc. Am. J.*, **67**, 606-611.
- Fischer, P., Kim, D.-H., Chao, W., Liddle, J.A., Anderson, E.H. & Attwood, D.T. (2006) Soft X-ray microscopy of nanomagnetism. *Materials Today*, **9** (1-2), 26-33.
- Garvie, L.A.J. & Buseck, P.R. (1998) Ratios of ferrous to ferric iron from nanometre-sized areas in minerals. *Nature*, **396**, 667-670.
- Gleber, S.-C., Knöchel, C., Thieme, J., Rudolph, D. & Schmahl, G. (2003) 3-D computer reconstruction of x-ray microscopy objects from stereo images. *Journal de Physique IV*, **104**, 639-642.
- Lehr, J. (1997) *Entwicklung, Charakterisierung und Anwendung von dreidimensionalen Bildgebungsverfahren für die Röntgenmikroskopie*. Shaker Verlag, Aachen.
- Hofmann, T., Baumann, T., Bundschuh, T., v.d.Kammer, F., Leis, A., Schmitt, D., Schäfer, T., Thieme, J., Totsche, K.U. & Zänker, H. (2003) Aquatische Kolloide I: Eine Übersichtsarbeit zur Definition, zu Systemen und zur Relevanz. *Grundwasser - Zeitschrift der Fachsektion Hydrogeologie*, **4**, 203-212.
- Hofmann, T., Baumann, T., Bundschuh, T., v.d.Kammer, F., Leis, A., Schmitt, D., Schäfer, T., Thieme, J., Totsche, K.U. & Zänker, H. (2003) Aquatische Kolloide II: Eine Übersichtsarbeit zur Probennahme, Probenaufbereitung und Charakterisierung. *Grundwasser - Zeitschrift der Fachsektion Hydrogeologie* **4**, 213-223.

Kirz, J., Jacobsen, C. & Howells, M. (1995) Soft X-ray microscopes and their biological applications. *Quarterly Reviews of Biophysics*, **28** (1), 33-130.

Larabell, C.A. & Le Gros, M.A. (2004) X-ray tomography generates 3-D reconstruction of the yeast, *Saccharomyces cerevisiae*, at 60-nm-resolution. *Mol. Biol. Cell*, **15**, 957-962.

Meyer-Lilse, W., Denbeaux, G., Johnson, L.E., Bates, W., Lucero, A. & Anderson, E (2000) The High Resolution X-ray Microscope, XM-1. AIP Conf. Proc., **507**, 129-

Niemann, B., Rudolph, D. & Schmahl,G. (1974) Soft X-ray imaging zone plates with large zone numbers for microscopic and spectroscopic applications. *Optics Communications*, **12**, 160-163.

Rhoton, F.E., Römkens, M.J.M., Bigham, J.M., Zobeck, T.M. & Upchurch, D.R. (2003) Ferrihydrite influence on infiltration, runoff and soil loss. *Soil Sci. Soc. Am. J.*, **67**, 1220-1226.

Schneider, G., Anderson, E., Vogt, S., Knöchel, C., Weiß, D., Le Gros, M.A. & Larabell, C.A. (2002) Computed tomography of cryogenic cells. *Surface Review & Letters*, **9**, 177-183.

Schwertmann, U. & Cornell, R.M. (2000) *Iron Oxides in the Laboratory – Preparation and Characterization*. Wiley-VCH, Weinheim, Germany.

Sparks, D. (1995) *Environmental Soil Chemistry*. Academic Press, San Diego, USA.

Susini, J., Joyeux, D. & Pollack, F. (Eds.) (2003) X-Ray Microscopy 2002. *Journal de Physique IV*, EDP Sciences, Grenoble, France.

Thieme, J., Schneider, G. & Knöchel, C. (2003) X-ray tomography of a microhabitat of bacteria and other soil colloids with sub-100 nm resolution. *Micron*, **34**, 339-344.

Weiß, D., Schneider, G., Niemann, B., Guttman, P., Rudolph, D. & Schmahl, G. (2000) Computed tomography of cryogenic biological specimens based on X-ray microscopic images. *Ultramicroscopy*, **84**, 185-197.

Wolter, H. (1952) Spiegelsysteme streifenden Einfalls als abbildende Optiken für Röntgenstrahlen. *Ann. Phys.* **6** (10), 94-114.